nature geoscience

SUPPLEMENTARY INFORMATION

https://doi.org/10.1038/s41561-019-0489-1

In the format provided by the authors and unedited.

Enhanced upward heat transport at deep submesoscale ocean fronts

Lia Siegelman[1,2,3]*, Patrice Klein[1,2,4], Pascal Rivière[3], Andrew F. Thompson[1], Hector S. Torres[2], Mar Flexas[1] and Dimitris Menemenlis[2]

[1]Environmental Science and Engineering, California Institute of Technology, Pasadena, CA, USA. [2]Jet Propulsion Laboratory, California Institute of Technology, Pasadena, CA, USA. [3]Université de Brest, CNRS, IRD, Ifremer, LEMAR, Plouzané, France. [4]Université de Brest, CNRS, IRD, Ifremer, LOPS, Plouzané, France. *e-mail: lsiegelman@caltech.edu

Enhanced upward heat transport at deep submesoscale ocean fronts - Supplementary Information

Lia Siegelman[1,2,3*], Patrice Klein[1,2,4], Pascal Rivière[3], Andrew F. Thompson[1], Hector S. Torres[2], Mar Flexas[1], and Dimitris Menemenlis[2]

[1]Environmental Science and Engineering, California Institute of Technology, Pasadena, CA, USA
[2]Jet Propulsion Laboratory, California Institute of Technology, Pasadena, CA, USA
[3]Univ. Brest, CNRS, IRD, Ifremer, LEMAR, Plouzané, France
[4]Univ. Brest, CNRS, IRD, Ifremer, LOPS, Plouzané, France
[*]lsiegelman@caltech.edu

Consistency between seal and satellite observations at meso- and submesoscale

The contribution of the vertical stratification to the SSH can be estimated by integrating the hydrostatic equation $\mathrm{d}p/\mathrm{d}z = -\rho g$. The SSH ($\eta$) referenced from $z = 0$ is then given by[1]

$$\eta = \frac{p'_b}{\rho_0 g} - \frac{p_a}{\rho_0 g} - \int_{-H}^{0} \frac{\rho'}{\rho_0} dz, \tag{1}$$

where p is the pressure, ρ the potential density, ρ_0 the reference potential density (1025 kg m^{-3}), ρ' the potential density anomaly ($\rho = \rho_0 + \rho'$), g the gravity of Earth, p_a the atmospheric surface pressure, H the depth of the ocean and $p'_b = p_b - \rho_0 g H$ the bottom pressure anomaly with p_b the ocean bottom pressure. The term $\int_0^\eta \rho'/\rho_0 \, dz$ has been neglected because $\eta \ll H$. The three terms on the right hand side of equation (1) represent respectively the contributions from the bottom pressure, the atmospheric pressure loading, and the steric height. The steric height (ζ) is computed with the seal dataset from the surface down to $H = 400$ m for dives reaching at least 400 m (3100 dives) as $\zeta_{400} = \int_{-400}^{0} \rho'/\rho_0 \, dz$. ζ_{400} is then compared to the SSH observed by altimetry.

SSH obtained from satellite data and mixed layer depth (MLD) and buoyancy anomalies, sampled by the seal, have a larger magnitude in the strongly turbulent region (Fig. 2) than in the weakly turbulent one (Extended Data Fig. 1i). Anticyclonic structures, or positive SSH anomalies, are associated with an increase in MLD and bowl-shaped positive buoyancy anomalies from the surface down to 400 m depth (Fig. 2 and Extended Data Fig. 1). Shallow MLD and negative buoyancy anomalies are associated with cyclonic structures, or negative SSH anomalies, confirming the fact that buoyancy anomalies compensate SSH anomalies. To further quantify this compensation over the water column, we have compared SSH with the depth-integrated buoyancy also called steric height. Since seal observations mostly sample the upper ocean, the steric height contribution has been estimated from surface down to 400 m (which concerns at least 35% of the dives) as $\zeta_{400} = \int_{-400}^{0} b dz$ with b the buoyancy (see Methods). As emphasized by the time-series in Fig. S1a (SSH in black and ζ_{400} in blue), SSH and steric height fluctuations correlate well over the entire trajectory, but only for scales smaller than 100 km. SSH reveals a large-scale signal ($\sim$1000 km) not present for ζ_{400}. This indicates that SSH at larger scales is likely compensated by the buoyancy field below 400 m and/or by bottom pressure, The contribution of ζ_{400} to SSH is no more than 30% as revealed by the linear regression coefficient of 3.58 linking the two-time series (not shown).

To remove this large-scale contribution and focus only on the meso/sub-mesoscale band, time-series of the horizontal gradients of SSH and ζ_{400} are computed (a gradient operator overemphasizes contribution of smaller scales). This is the equivalent of comparing horizontal currents from SSH using the geostrophic approximation, with those explained by the buoyancy field contribution in the water column using the thermal wind balance[1]. The two time-series are now closer in terms of amplitude differences (Fig. S1b). ζ_{400} gradients statistically explain almost 75% of the SSH gradients as revealed by the linear regression coefficient of 1.35 linking the two time-series (not shown). This further emphasizes the consistency between the two independent datasets at meso/sub-mesoscale despite their different spatial resolution. The main differences concern the extrema of SSH gradients (mostly located on the eddy edges) that overcome those of ζ_{400} gradients by a factor of two to three. This suggests the steric height is not integrated deep enough to capture SSH in the upper mesoscale band and therefore that dynamics of this band affects at least the first 400 m below the surface.

Link between the strain field, Finite Size Lyapunov Exponents and lateral gradients of buoyancy

As illustrated in Fig. 3a, buoyancy anomalies embedded in a strain field are elongated in one direction and compressed in the perpendicular direction. This mechanism can be understood in terms of particle dispersion, and thus in terms of Finite Size Lyapunov Exponents (FSLE); two particles, initially close and embedded in a strain field, become quickly separated in one particular direction (the stretching direction, in red in Figs 3a and 4a). As such, the time scale of their separation can be characterized by λ^{-1} (see equation 2 in Methods), with large λ being indicative of an intense strain field. More precisely, FSLE characterize both the time scale (via the largest FLSE eigenvalue λ) and the direction (via the FSLE eigenvector associated to λ) of the elongation of buoyancy anomalies.

Thus, the time scale λ (shown in the colorbar of Fig. 4a for instance) can be used to characterize the production of buoyancy gradient expressed in the RHS of the omega equation (equation 3 in Methods). In particular, the intersection of intense compressing and stretching FSLE lines, respectively in blue and red in Figs 3a and 4a, identify Lagrangian hyperbolic points, where particles (or tracers) are simultaneously being stretched along one direction and compressed along the other one. Areas surrounding hyperbolic points are particularly prone to frontogenesis.

Vertical velocities underestimation

At steeply titled isopycnals' fronts, the vertical velocity field is more accurately captured by the full omega equation, known as the Sawyer-Eliassen (SE) equation, than by its QG version[2,3]. The 2-D (x,z) SE equation, assuming the front is embedded in a pure strain field and diffusive processes are negligible, reads[2]:

$$N^2\frac{\partial^2\psi}{\partial x^2}+F^2\frac{\partial^2\psi}{\partial z^2}+2S^2\frac{\partial^2\psi}{\partial z\partial x}=2u_x b_x, \tag{2}$$

with ψ a meridional streamfunction related to the ageostrophic circulation (i.e. defined as $v_a=-\frac{\partial\psi}{\partial z}$, $w=\frac{\partial\psi}{\partial x}$, with v_a the ageostrophic component of the meridional component of the horizontal velocity field. $N^2=N^2(x,z)$, $S^2=-b_x$ and $F^2=f(f+\frac{\partial v}{\partial x})$, where $\frac{\partial v}{\partial x}$ is the relative vorticity associated with the front[3].

Compared with the QG version (equation 3 in Methods) rewritten in the form of the ageostrophic stream function, equation (2) involves $F^2=f(f+\frac{\partial v}{\partial x})$ instead of f^2 as well as $N^2(x,z)$ instead of $N^2(z)$. In addition, equation (2) involves the extra term $2S^2\frac{\partial^2\psi}{\partial z\partial x}$. A dimensional analysis, using L and D as respectively the horizontal and depth scales of the front, indicates that this extra term is of the order of Ri^{-1}, with Ri the Richardson number, compared to the other two terms on the LHS[2,3]. Since Ri^{-1} is not small but close to one at locations of sharp fronts, this term should not be ignored. Nevertheless, a real solution for equation (2) exists if and only if $F^2N^2-S^4>0$. This condition can be written as $f^2N^2(1+\text{Ro-Ri}^{-1})>0$, with Ro the Rossby number. As such, it places a strong constraint on Ri^{-1}, which is postive and has to be smaller than |1+Ro|. This leads to a limitation of the steepness of the front and also to a limitation of the importance of the S^2 term relatively to others.

However, we do not have access to F^2 and in particular to $\frac{\partial v}{\partial x}$, the along-front relative vorticity, that can be of order f. SSH observations have a spatial resolution too low to resolve $\frac{\partial v}{\partial x}$ at these scales. This is why we use the QG version (equation 3 in Methods). Nevertheless, many studies, starting with Hoskins (1982)[4] and more recently confirmed by Hakim and Keyser (2001)[2], emphasize that the SE and QG solutions are qualitatively similar when the condition $F^2N^2-S^4>0$ is met. In particular, the SE and QG ageostrophic circulation, and therefore the w-field, have the same sign. What differs is the amplitude of the w-field, which is larger in the SE solution, as well as the shape of the ageostrophic circulation, which is more tilted and oriented parallel to the isopycnals in the SE solution. Thus, the QG omega solution gives the correct sign for w but the magnitude may be underestimated at low Ri.

This underestimation can however be quantified using the analytical solutions for the QG and SE versions of the omega equation derived in Hakim and Keyser (2001)[2]. These authors show that $w_{SA}\sim w_{QG}[\frac{PV_{QG}}{PV_{PE}}]^{1/2}$ with w_{SA} and w_{QG} respectively the solution of the QG and SA equations and PV_{QG} and PV_{PE} respectively the QG potential vorticity and the Ertel potential vorticity. Using the approximations $PV_{QG}\sim fN^2$ and $PV_{PE}\sim fN^2[1-Ri^{-1}]$, as detailed by Thomas et al. 2008[3], leads to $[\frac{PV_{QG}}{PV_{PE}}]^{1/2}=[\frac{1}{1-Ri^{-1}}]^{1/2}$. When $Ri=2$, which corresponds to the strongest fronts in the seal measurements (see main text), we get $w_{SA}\sim 1.4\times w_{QG}$. In other words, the maximum w-values found in our study should be closer to 140 m/day than to 100 m/day.

Dominance of frontogenesis versus frontolysis understood via the direct cascade of potential energy

The classical frontogenesis process[5] emphasizes that the increase tendency of a buoyancy gradient embedded in a strong strain field is balanced by a vertical velocity field that tends to decrease this buoyancy gradient (black arrows in Fig. 3b). The reason is that a buoyancy gradient increase destroys the thermal wind balance and this balance is restored by the emergence of the vertical velocity field. These mechanisms lead to the omega equation (see Methods section "Vertical velocities"). As illustrated in Fig. 3b, the frontogenesis process leads to an upward vertical heat flux (red arrows in Fig. 3b) because of the positive correlation between temperature and vertical velocities anomalies.

On the other hand, the frontolysis process, or the destruction of front, occurs when the strain rate decreases and/or changes its direction. As a consequence, the buoyancy gradient relaxes, which is then balanced by a vertical velocity field (and therefore a vertical heat flux) in the opposite direction for the same reason as before (thermal wind balance). The frontolysis process is also captured by the omega equation and is associated with a downward vertical heat flux because of the negative correlation between temperature and vertical velocities anomalies (Fig. 5c). Frontogenesis (frontolysis) processes explain occurrences of positive (negative) vertical heat fluxes displayed in Fig. 5c and Extended Data Fig. 5b.

However, a well-known property of mesoscale eddy turbulence is the direct cascade of potential energy driven by the background strain field. The direct cascade refers to the creation of buoyancy anomalies at smaller and smaller scales and thus to the continuous production of submesoscale fronts[6]. This is why frontogenesis processes statistically dominate frontolysis ones, as can be seen in Fig. S2c where positive buoyancy fluxes are more numerous and of greater magnitude than negative ones. As a consequence, we propose that the dominance of positive vertical heat fluxes at submesoscale as demonstrated in the main text is consistent with the strong background eddy field (Fig. 5f).

Numerical simulation comparison

The vertical velocity field and vertical heat transport (VHT) calculated from the observations are compared to the same fields obtained from a high-resolution numerical simulation in the Kerguelen area in late spring-early summer (November 2011) performed with the Massachusetts Institute of Technology general circulation model (MITgcm). This high-resolution simulation has a horizontal resolution of 1/48°, 90 vertical levels and 10 minute outputs and is described in many papers (see for example Su *et al.* (2018)[7]). The model domain is 45°S–55°S/ 85°E–95°E (or $\sim 1000 \times 1000$ km). This domain is embedded in the MITgcm LLC 4320 global numerical simulation performed at the same resolution but with hourly outputs[7]. Boundary conditions and forcings are supplied by the global simulation.

Vertical sections of daily averaged vertical velocities and vertical heat transport obtained from this simulation are presented in Extended Data Fig. 5. At depths of 100–600 m, intense vertical velocities with a width of 5–10 km are present below the mixed layer and reach 300 m/day. Similar features are observed for vertical heat transport with values locally reaching 4000 W/m^2. Two-dimensional slices (x,y) of vertical heat transport averaged over 10 days are shown in Extended Data Fig. 6 at 50 and 200 m. This Fig. clearly highlights that the organization of VHT is driven by the background mesoscale strain field, intensified on the eddy edges. This Fig. also shows the dominance of positive VHT in the domain as well as its intensification at depth. Finally, Extended Data Fig. 7 presents the domain-averaged VHT over one month, which reveals similar - although larger - values than the ones derived from the observational data. Overall, the similar shape, distribution within the water column, and magnitude of both quantities in the model and in the observations strengthen the results presented in this study, and further highlight the impact of deep reaching ocean fronts on oceanic heat transport.

References

1. Vallis, G. K. *Atmospheric and oceanic fluid dynamics* (Cambridge University Press, 2017).
2. Hakim, G. & Keyser, D. Canonical frontal circulation patterns in terms of green's functions for the sawyer-eliassen equation. *Q. J. Royal Meteorol. Soc.* **127**, 1795–1814 (2001).
3. Thomas, L. N., Tandon, A. & Mahadevan, A. Submesoscale processes and dynamics. *Ocean. modeling an Eddying Regime* **177**, 17–38 (2008).
4. Hoskins, B. J. The mathematical theory of frontogenesis. *Annu. review fluid mechanics* **14**, 131–151 (1982).
5. Hoskins, B. J. & Bretherton, F. P. Atmospheric frontogenesis models: Mathematical formulation and solution. *J. Atmospheric Sci.* **29**, 11–27 (1972).

6. Salmon, R. Baroclinic instability and geostrophic turbulence. *Geophys. & Astrophys. Fluid Dyn.* **15**, 167–211 (1980).

7. Su, Z., Wang, J., Klein, P., Thompson, A. F. & Menemenlis, D. Ocean submesoscales as a key component of the global heat budget. *Nat. communications* **9**, 775 (2018).

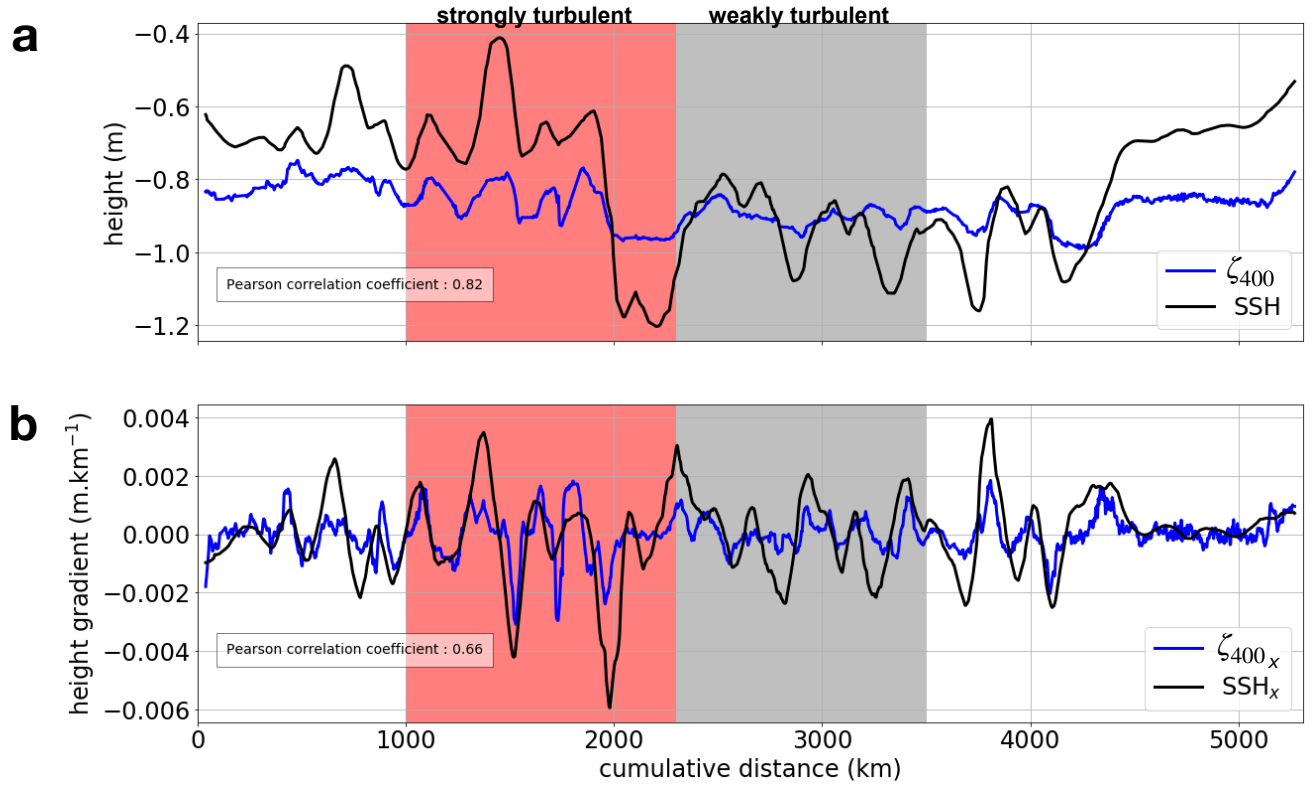

Supplementary Fig. S1. SSH and steric height (ζ_{400}). a) Time series of satellite SSH (black line) along the seal's path and steric height (ζ_{400}, blue line) calculated from the SES dataset down to 400 m. b) Time series of the lateral gradients of SSH (SSH_x, black line) and steric height (ζ_{400_x}, blue line). On both panels, the red (grey) zone corresponds to the strongly (weakly) turbulent area of Fig. 2(S1i).

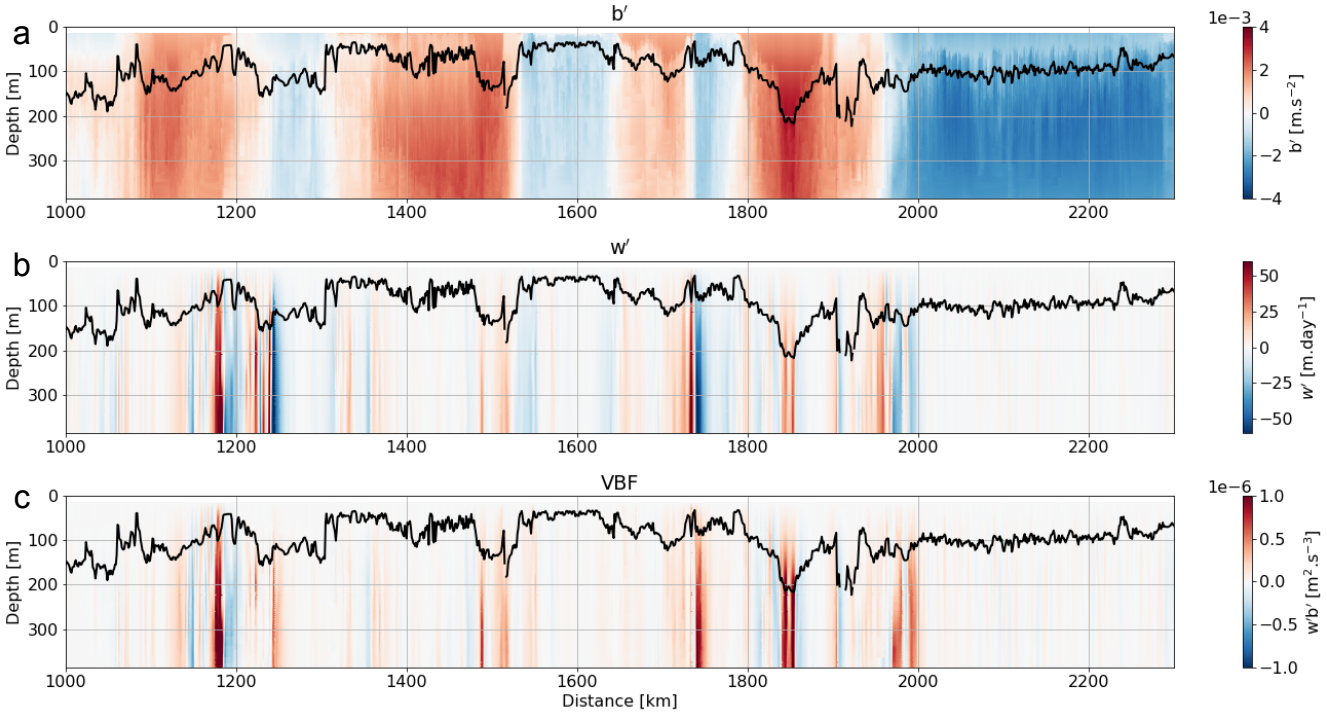

Supplementary Fig. S2. Buoyancy and temperature anomalies and vertical buoyancy fluxes from seal and satellite data Same as Fig. 5 but for buoyancy. a) Vertical section of buoyancy anomaly sampled by the seal. b) Vertical section of vertical velocity anomaly derived from the seal and satellite data by solving the omega equation (see main text and Methods). c) Vertical section of vertical buoyancy flux (or transport, VBF) defined as $w'b'$, with w' and b' are the anomalies of vertical velocity and buoyancy, respectively. The mixed layer depth is shown in bold black. From panel c) it is clear that frontogenesis (positive VBF, in red) dominates frontolysis (negative VBF, in blue).